Thermal analysis of the girth weld of an elastomeric diaphragm tank

J. Vincent, J.M. Carella, A.P. Cisilino *

INTEMA, Faculty of Engineering, University of Mar del Plata-CONICET, Av. Juan B. Justo 4302, Mar del Plata, Argentina

ABSTRACT

The finite-element thermal analysis of the welding process of a titanium-alloy tank with an elastomeric diaphragm is described. The analysis takes into account the latent heat due to phase changes, the dependence of the material properties with temperature and the effects of the convection in the weld pool. The model is calibrated and validated by comparing its predictions with experimental results from the welding of AISI 304 specimens. The comparison between the model and the experimental results is made in terms of the temperature fields and the dimensions of the weld molten pool. The time evolution of the temperature in the experiments is monitored using thermocouples and a thermographic camera. The molten pool dimensions are measured via macro etching. The girth weld of the tank is analyzed for various hypotheses for the efficiency of the contact heat conduction between the hemispheres and the diaphragm-retaining ring. The results show the convenience to include a heat sink to the welding setup in order to guarantee the thermal integrity of the elastomeric diaphragm.

© 2013 Elsevier B.V. All rights reserved.

1. Introduction

Positive expulsion devices are extensively used in spacecraft secondary propulsion systems. Secondary propulsion systems are used in spacecrafts in maneuvers of reduced thrust level, such as station keeping and orbit control and attitude control (Moss and Stark, 2003). Positive expulsion devices use a pressure differential to expel propellant from its storage vessel. In mono-propellent systems the fuel is typically hydrazine, which is sprayed onto a catalyst bed that thermally decomposes the liquid to produce expanding and accelerating gases in a nozzle for trust.

Positive expulsion devices include diaphragms, bladders, pistons or bellows-based systems for fluid control and delivery (Ballinger et al., 1995). One of the most practical devices is diaphragms tanks, which use elastomeric materials for an effective barrier between the pressurant gas and liquid propellant. Diaphragm tanks are usually spherical in the pursuit of expulsion efficiency; however, they have also been produced with other geometries like ellipsoids, hemispherical heads with cylindrical center sections, ellipsoidal heads with cylindrical center sections and with tapered cylindrical sections. Tank sizes could range from 220 mm to 1200 mm and their are made of Ti–6Al–4V alloy (Ballinger et al., 1995). The material of the diaphragm is a cross-linked ethylene–propylene–diene thermopolymer with a curing temperature $T_c = 170\,°C$.

Fig. 1(a) illustrates a scheme of the spherical tank assembly that is object of this work. The diaphragm is sealed to the pressure shell using a metallic retaining ring. The two hemispheres and the retaining ring are joined together via a single gas-tungsten-arc-welding (GTAW) girth weld. Fig. 1(b) depicts a scheme of the girth weld joint. Since considerable heat will be locally generated during welding, it must be ensured that the diaphragm does not attain the rubber curing temperature in order to avoid its degradation.

It is presented in this paper a thermal analysis of the girth weld joint to assist the development of a welding process that preserves the integrity of the rubber diaphragm. The analysis comprises finite element (FE) modeling and experimental testing. Experimental data is obtained from welds performed on AISI 304 plates, in which the temperature is monitored using thermocouples and a thermographic camera. AISI 304 was chosen for these tests because it possesses thermal properties similar to those of the titanium alloy, but it has a lower cost. The experimental results are used for the FE model calibration and validation via the comparison of the temperature fields and the dimensions of the weld molten pool. Finally, the tuned model is used for the analysis and design of the girth weld of the titanium-alloy tank.

2. Modeling aspects

Lindgen (2006) proposed a five-level classification of the welding simulations based on the accuracy level: reduced, basic, standard, accurate and very accurate. Considering the scope of this work, which is the prediction of the transient temperature field in the zone near (but not immediately adjacent) to the weld pool, the FE models are designed to fulfill the requirements of *accurate simulations*.

Following well established approaches (see for example, Goldak et al., 1986 and Lindgen, 2006) the simulations in this work

* Corresponding author. Tel.: +54 (223) 4816600.
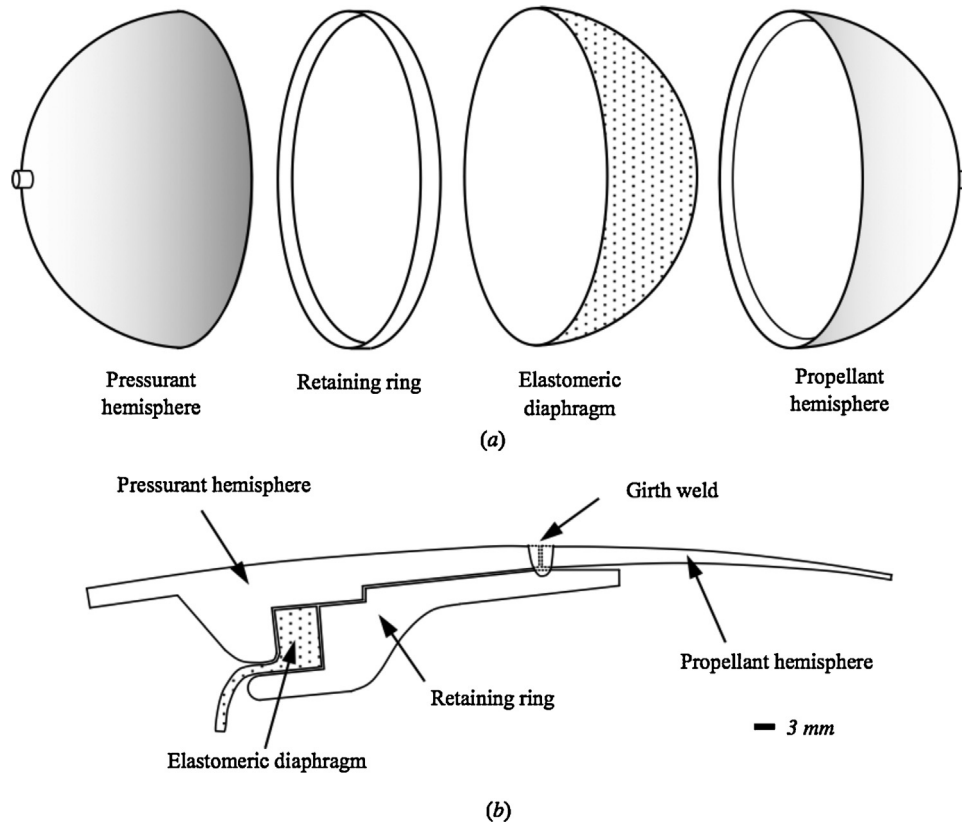 *E-mail address:* cisilino@fi.mdp.edu.ar (A.P. Cisilino).

Fig. 1. Elastomeric diaphragm tank: (a) mounting scheme and (b) detail of the girth weld joint.

consider only the weld thermal phenomena, and they incorporate all the physics of the welding process via empirical heat input models. The simulations account for the latent heat due to phase changes, the dependence of the thermal properties on temperature and the effects of the convection in the weld pool. The heat input is calibrated based on experimental data. The implementation details are reported in the next sections.

2.1. Heat input

The heat input is modeled using a Gaussian distribution of the heat flux. The heat flux is imposed over a circular surface centered at the position of the weld arc using

$$q(r) = q_m \cdot e^{-(r/(2\sigma^2))}, \tag{1}$$

where q_m is the maximum (peak) value of the heat flux at the center of the distribution, σ is the standard deviation and r is the radial distance from the center of the distribution. The maximum value of the heat flux can be related to the electric-arc power, P, via

$$q_m = \frac{P}{2\pi\sigma^2}. \tag{2}$$

The expression for the arc power in terms of the arc voltage, E, and current, I, is

$$P = \eta EI, \tag{3}$$

where η is the heat-transfer efficiency.

By using the relationship between voltage and current for power sources intended for GTAW due to Grist et al. (1993),

$$E \ [\text{V}] = 13 + 0.012 \cdot I \ [\text{A}], \tag{4}$$

together with the results in (2) and (3), the heat flux distribution in Eq. (1) can be rewritten as follows:

$$q(r) = \frac{\eta EI}{2\pi\sigma^2} \cdot e^{-(r/(2\sigma^2))}, \tag{5}$$

where the values for σ and η will be calibrated using experiments.

2.2. Heat losses and contact conductance

2.2.1. Convection heat loss
The convection heat loss to the air is modeled using the well known Newton's law,

$$q_{conv} = h(T_w - T_\infty), \tag{6}$$

where h is the heat-loss coefficient, T_w is the surface temperature of the specimen and T_∞ is the temperature of the environment.

The value of the heat-loss coefficients as a function of the surface temperature for the two geometries analyzed in this work, the vertical plate and the sphere, were computed following standard procedures given in Ozisik (2002) and Charmchi and Martin (1989). The results are plotted in Fig. 2.

2.2.2. Radiation heat loss
The radiative heat transfer is governed by the Stefan–Boltzmann law (Martin and Blanco-Muriel, 1989),

$$q_{rad} = e \cdot K(T_w^4 - T_\infty^4), \tag{7}$$

where K is the Stefan–Boltzman constant and e is the total emissivity of the surface. Following Ozisik (2002) and Martin and Blanco-Muriel (1989), the value $e = 0.5$ is adopted for the metallic surfaces.
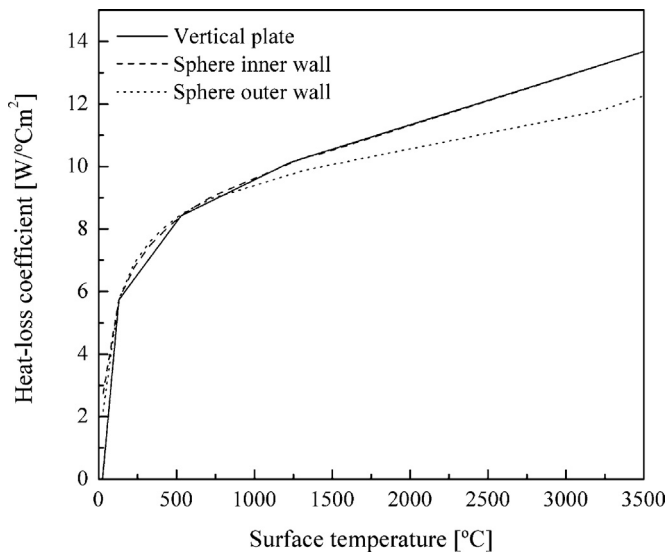
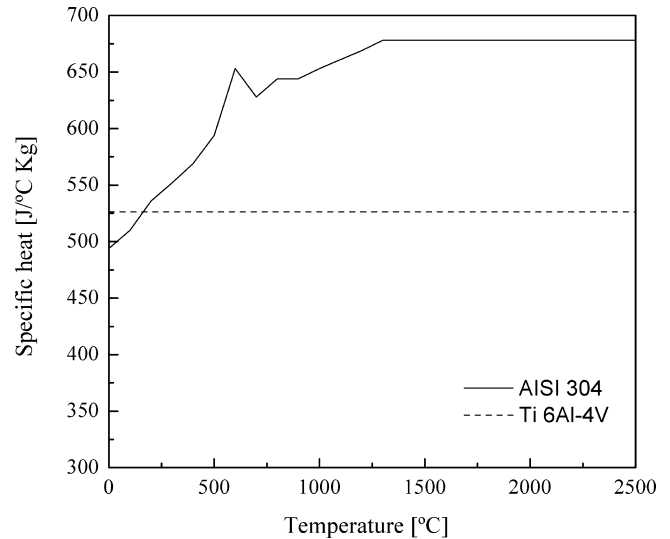**Fig. 2.** Heat-loss coefficients as functions of the surface temperature.

Fig. 4. Specific heats as functions of temperature.

2.2.3. Contact conductance

A simplified model for the contact conductance is used (Guyer and Golay, 1989),

$$q_{cont} = k_c(T_{w_1} - T_{w_2}), \qquad (8)$$

where k_c is the thermal conductance coefficient and T_{w_1} and T_{w_2} are the temperatures of the two surfaces into contact. The value of k_c is very difficult to set *a priori*, as it depends on many factors such as the contact pressure and the surface roughness and cleanliness. A number of hypotheses for k_c will be evaluated for the model of the tank.

2.3. Material models

Fig. 3 depicts the thermal conductivities of AISI 304 and Ti–6Al–4V as functions of temperature. Data bellow the solidus temperature for AISI 304 ($T \leq 1399\,°C$) are from Pehlke et al. (1982), while data for Ti–6Al–4V ($T \leq 1604\,°C$) are from the data sheet by Carpenter Technology Corporation (2000). Using a standard approach (see for example Lombera et al., 1989 and Goldak and Akhlaghi, 2005), the effects of the convection in the weld
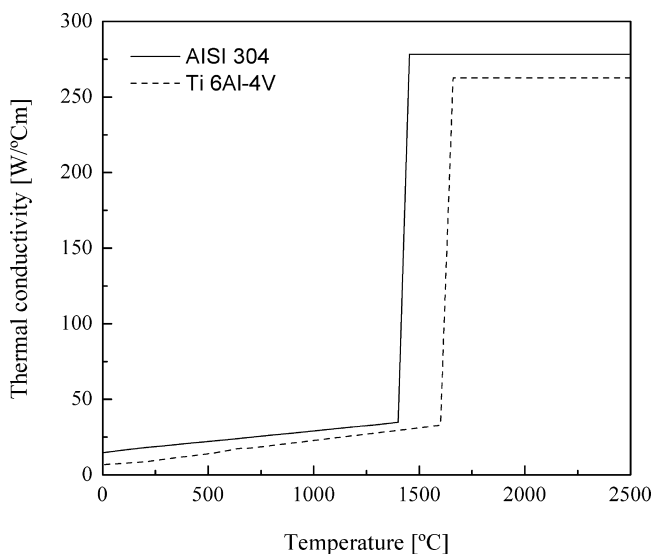

Fig. 3. Thermal conductivities as functions of temperature.

pool due to the fluid flow are incorporated into the model by increasing 8 times the conductivity of the liquid phase. This resulted in [k = 278.4] W/°C m, for the AISI 304 at $T > 1454\,°C$ and [k = 262.8] W/°C m for the Ti–6Al–4V at $T > 1660\,°C$. The conductivities are interpolated linearly in the range $T_{solidus} < T < T_{liquidus}$.

The data for the specific heat as a function of temperature are plotted in Fig. 4. The data for the AISI 304 is from Pehlke et al. (1982). For the Ti–6Al–4V, the constant specific heat [c = 526.3] J/°C kg from MatWeb (2012) is used, as it was not possible to find temperature-dependent data. It is assumed that latent heats are evenly distributed during solidification/melting in the range $T_{solidus} < T < T_{liquidus}$. Latent heats are [$L$ = 290] kJ/kg for the AISI 304 and [L = 419] kJ/kg for the Ti–6Al–4V.

3. Finite element modeling

The FEA is performed using Abaqus Standard (2009). The geometry of the model for the AISI 304 plates is shown in Fig. 5 together with its finite element discretization. The symmetry of the problem allows for the discretization of half of the model only. The discretization strategy was devised based on preliminary tests for which the analytical solutions of the temperature field due to Tsai and Tso (1993) were used as references. The model discretization is divided into four regions. Region #1, the closest to the weld line, is discretized using quadratic hexahedral elements (DC3D20). In order satisfy the requirements of an *accurate analysis*, at least four elements are accommodated along the semi-axis of the Gaussian heat source (Lindgen, 2006). The mesh is progressively coarser in Regions #2, #3 and #4, which are further from the weld line. Region #2 is discretized using quadratic hexahedral elements, while linear hexahedral elements (DC3D8) are used for Regions #3 and #4. In order to keep the computational cost to the minimum, non-confirming discretizations are used at the interfaces between the regions, where the continuity in the solution is enforced using the *TIE command. The resulting discretization consists of 12,270 elements and 57,820 nodes. The same strategy is used for the discretization of the model of the tank. This is illustrated in Fig. 6, where the gradual densification of the FE mesh towards the weld line can be observed. The mesh of the model of the tank consists of 25,350 elements.

The models are solved in two *STEPS. The boundary and initial conditions are set in the first step (steady-state). In the second step (transient), the heat source moves to simulate the welding.
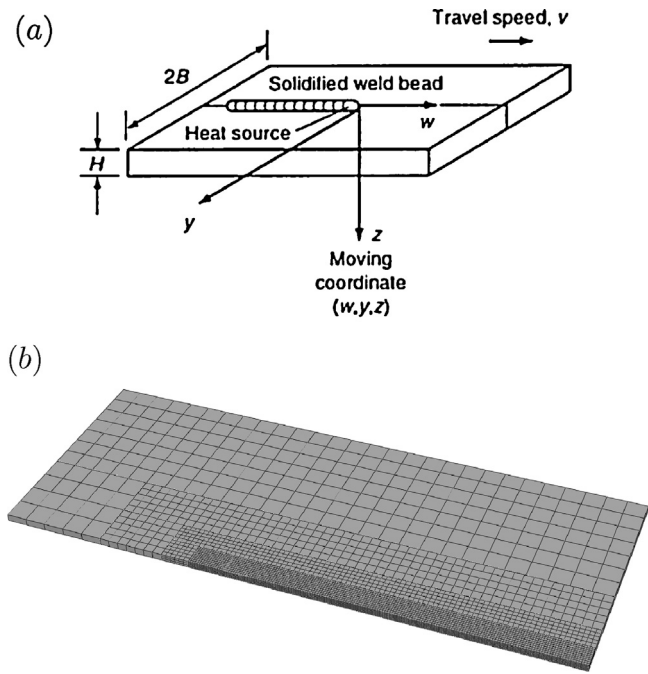
Fig. 5. (a) Schematic of the welding thermal model (figure reproduced from Tsai and Tso, 1993) and (b) finite element discretization.

In essence, the movement of the source consists in a procedure that activates and deactivates in sequence a series of discrete heat sources placed along the weld line. The n discrete Gaussian heat distributions (see Section 2.1) are placed along the weld line with a separation l_0 between them, see Fig. 7a. The heat distributions are created using the *ANALYTICAL FIELD command. The activation and deactivation of the heat distributions is done via a sequence of *AMPLITUDE commands, which have bilinear variations during the time intervals $2\tau_0$ and maximums at $t = i\tau_0 (i = 1, 2, \ldots n)$, see Fig. 7b. The values for l_0 and τ_0 set the magnitude of the weld speed, $v = l_0/\tau_0$. Results from preliminary tests showed that it was important that the procedure mimics a continuous and smooth movement for the source in order to achieve accurate results, so

Fig. 6. (a) General view of the FE model of the tank girth weld, and (b) detail of the model cross-section.
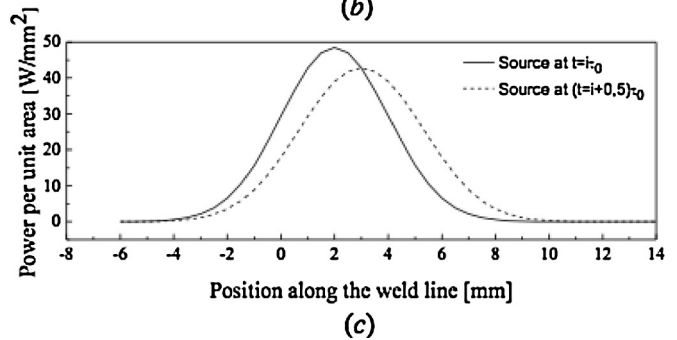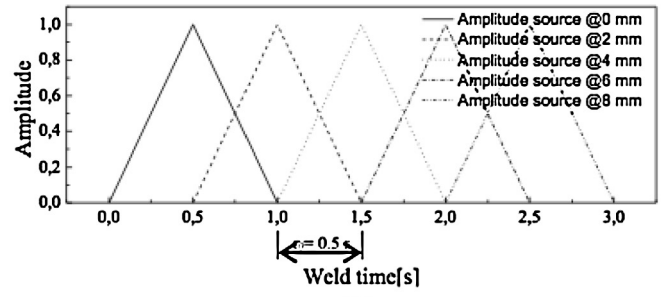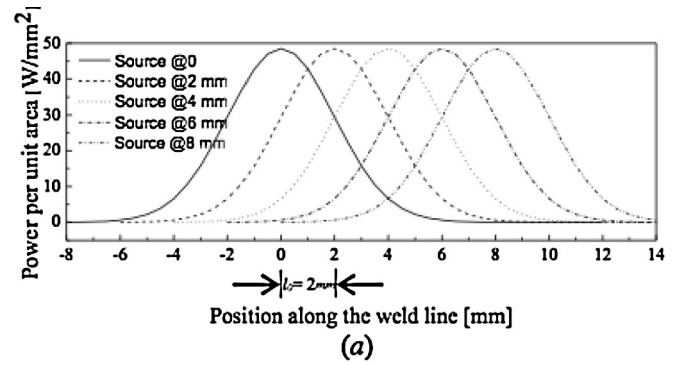

Fig. 7. Procedure for the simulation of the heat-source movement: (a) Gaussian heat distributions, (b) amplitude curves and (c) extreme values of the heat source. Weld parameters of the plots are those of the case W#3 in Table 1.

l_0 and τ_0 have to be properly chosen in order to minimize the fluctuations in the heat input. The plots in Fig. 7 are for a typical set of welding parameters used in this work. Fig. 7c illustrates the extreme values for the heat source. They occur at $t = i\tau_0$, this is, when the position of the source coincides with the center of a Gaussian heat distribution, and at $t = (i + 0.5)\tau_0$, this is, when the source is midway between two consecutive Gaussian heat distributions. The maximum difference between the discretized heat source and the analytical Gaussian distributions is −12% in the peak value and 11% in the standard deviation, what results in a −5% difference in the heat input. Preliminary tests showed that this difference is acceptable for the accuracy level intended for this work. Convergence analyses allowed to conclude that using 2 elements to discretize l_0 and 6 time increments to discretize τ_0 are enough to produce accurate results. This discretization criterion will be used for all the analyses in this work.

Convection and radiation boundary conditions are specified using the data in Section 2.2. For the model of the tank, contact conductance is specified in the contact zones between the hemispheres and the retaining ring. On the other hand, the metal–rubber interface between the hemispheres and the diaphragm is assumed isolated because it was difficult to find a reliable value for the contact conductance. This assumption is justified by the relative low conductivity of the rubber with respect to the titanium alloy (from 20 to 40 times lower). In any case, to omit the heat transfer to
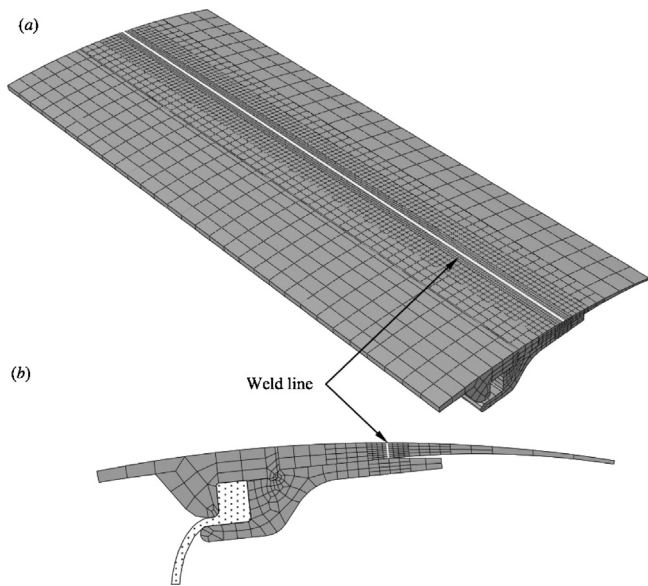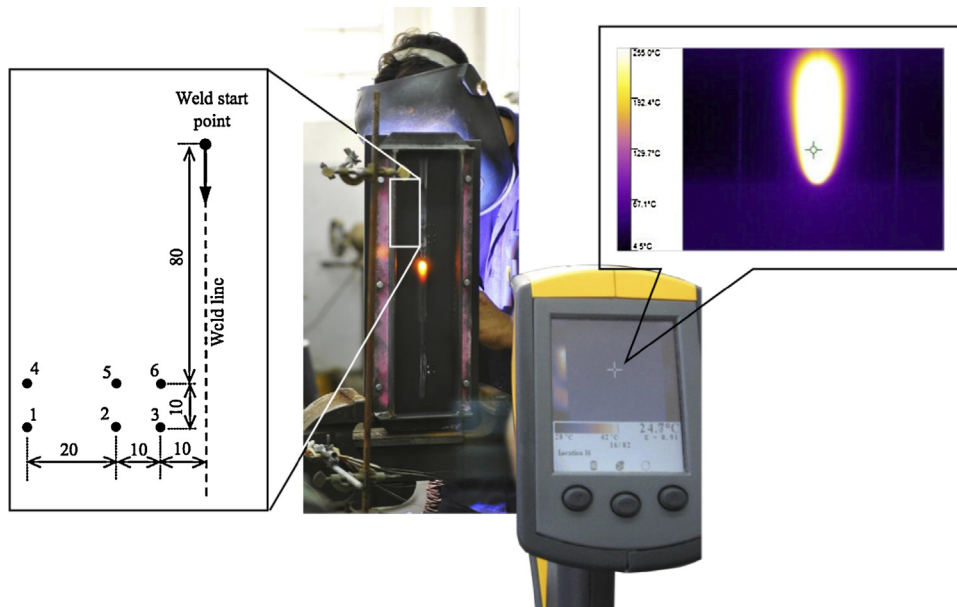
Fig. 8. Experimental set-up: welding of the plates in descending vertical position while monitoring temperatures using thermocouples (thermocouples arrangement is depicted on the left with the dimensions in mm) and the thermographic camera from the backside.

Table 1
Summary of welding parameters.

Welding Parameters	W#1	W#2	W#3
Current [A]	70	134	155
Voltage [V]	13.84	14.61	14.86
Welding time [s]	48	35	31
Weld line length [mm]	120	135	120
Velocity [mm s^{-1}]	2.50	3.86	3.87

the diaphragm will conduct to conservative results, since higher temperatures will be predicted for the tank wall.

Temperature-dependent material properties for conductivity, specific heat and latent heat are specified in tabular form using the data presented in Section 2.3.

4. Experimental aspects

Square butt joints were fabricated by welding two AISI 304 plates with dimensions $L \times B \times H = 500\,\text{mm} \times 100\,\text{mm} \times 3.17\,\text{mm}$ (see Fig. 5). The welds were manufactured manually by a professional welder using a Rehem GTAW Tiger 170A machine with a 1.6-mm electrode. The welds were autogenous, i.e., no filler wire was used. The three sets of welding parameters in Table 1 were used. Welding time was measured using a manual chronometer. Errors in the weld velocities were estimated considering a measurement error of 1% in the weld length and of 2% in the weld time. All the welds were practiced in descending vertical position. A metal frame was used to hold the plates in place and to avoid the specimen distortion.

In situ temperature measurements were made using K-type thermocouples and an infrared thermographic camera Fluke Ti-30. Thermocouples were welded in the heat affected zone using the arrangement depicted in Fig. 8. The transient analytical solution due to Tsai and Tso (1993) for the weld temperature field was used to select the best positions for the thermocouples. The back faces of the plates (these are the faces opposite to the welds) were painted matte black to maximize and homogenize their infrared emittances. The resolution of the thermal images was 120 pixels × 160 pixels, with a single temperature value assigned to each pixel.

An auxiliary experiment was performed to determine the value of the emittance of the black surface. One of the plates was heated using an electric heat gun meanwhile the temperature field was monitored using the thermocouples and the thermographic camera. A least-square analysis was performed to optimize the value of the emittance that minimized the difference between the two sets of measurements. The optimum value for the emittance $e = 0.91$ was found, which resulted in differences less than 4% in the range $40\,^\circ\text{C} \le T \le 160\,^\circ\text{C}$.

Dimensions of the molten pool were measured using macro etch testing of the cross sections. Samples were cut every 10 mm along the weld line using a bandsaw, their surfaces were polished and then etched using Vilella. The molten pool dimensions were measured using a measuring magnifier. As an example, the measurements for weld W#1 are plot in Fig. 9. It can be observed that after the transient associated to the weld start, the molten pool dimensions became stable when the weld had advanced around 60 mm. This behavior was the same for all the specimens, what confirmed that all the welds had achieved their steady-state regimes. The molten pool dimensions reported in next sections are those at the steady-state regimes.

5. Results and discussion

5.1. AISI 304 plates

The experimental data for the temperature field and the molten pool dimensions were used to calibrate the finite element models. Two parameters were calibrated: the standard deviation of the Gaussian heat source, σ, and the heat-transfer efficiency, η. The calibration included a sensitivity analysis to account for the effects of the measurement errors in the welding velocities. Satisfactory predictions of the size of the molten pool and the thermal fields were achieved for $\sigma = 2\,\text{mm}$ and the following efficiencies for the three welds: $\eta_{\text{W#1}} = 0.30$, $\eta_{\text{W#2}} = 0.40$ and $\eta_{\text{W#3}} = 0.53$.

The comparison between the experimental and FEM temperature results are plotted in Figs. 10 and 11. Fig. 10 depicts the comparison between the thermal histories at the positions of the thermocouples T#2 and T#6 (see Fig. 8) for weld W#2. Fig. 11 compares the temperature profiles along the *y*-direction at distances
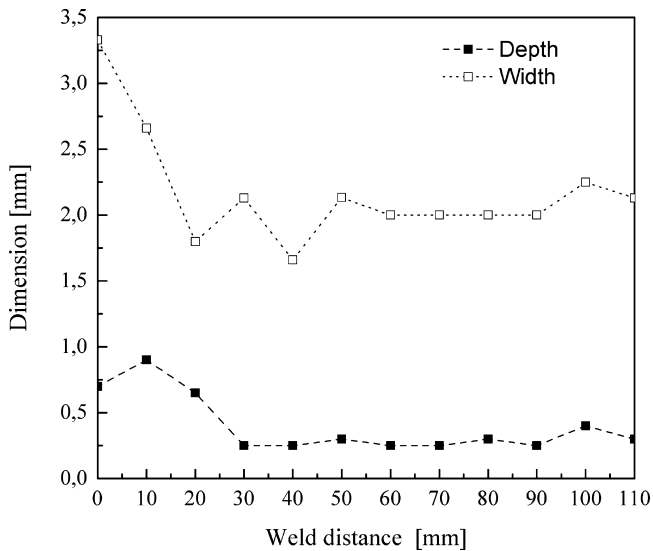
Fig. 9. Molten pool dimensions as a function of the distance to the weld start point for weld W#1.

Fig. 11. Comparison of the measured and FEA temperature profiles at various distances behind the heat source after 40 s since the start of weld W#3. Error bars indicate the sensitivity of the results to the error in the weld velocity.

Table 2
Molten pool dimensions [mm] measured in the experiments and predicted by the FE models.

| Weld | Experiment | | FEA model | | | |
| | | | $\sigma = 1$ mm | | $\sigma = 2$ mm | |
	Width	Depth	Width	Depth	Width	Depth
W#1	2	0.25	1	0.125	0	0
W#2	4.7	1.5	–	–	4.2	1.05
W#3	5.3	2	5.5	>3.17	5.8	1.8

$w = -8$, -16 and -32 mm behind the heat source 40 s after the start of W#3. The experimental results in Fig. 11 are from the thermographic camera. The error bars indicate the sensitivity of the results to the error in the welding velocity. It can be observed that the experimental measurements lie within the dispersion of their numerical predictions.

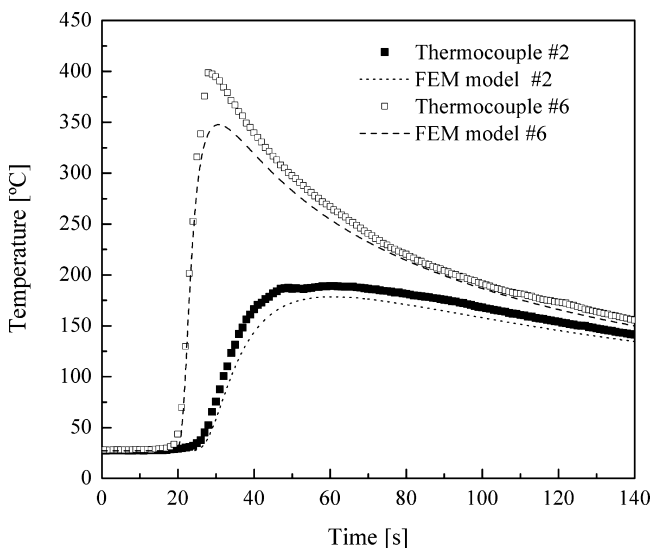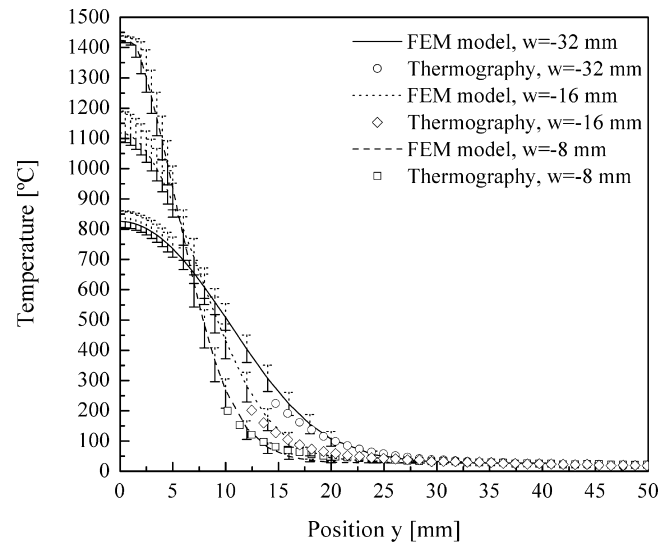The results for the size of the molten pool are reported in Table 2. The shapes of the molten pools in the FE models were determined using the positions of the liquidus-temperature isotherm. The FE predictions exhibit a strong dependence with the welding parameters, what makes difficult to find a single set of parameters that results, at the same time, in accurate predictions of both, the molten-pool size and the temperature field. Somehow, this was an expected outcome, since as it was expressed earlier in Section 2, the physics of the welding process in the pool were incorporated into the simulation using empirical models. Since the focus of this work is on the prediction of the temperature field in the heat affected zone, the model was calibrated to attain the best performance in this aspect. The best fit of the results for the welds #W2 and W#3 were prioritized since, as they present the larger penetrations, they better mimic the welding process to be used for the construction of the tank. The above considerations justify the selection of the dispersion $\sigma = 2$ mm for the heat source.

5.2. Tank girth weld

The parameters for W#3 (see Table 1) were selected for the tank girth weld. Due to the difficulty and uncertainty to set the contact conductance coefficient for the interface between the hemisphere inner walls and the retaining ring, two limiting hypotheses
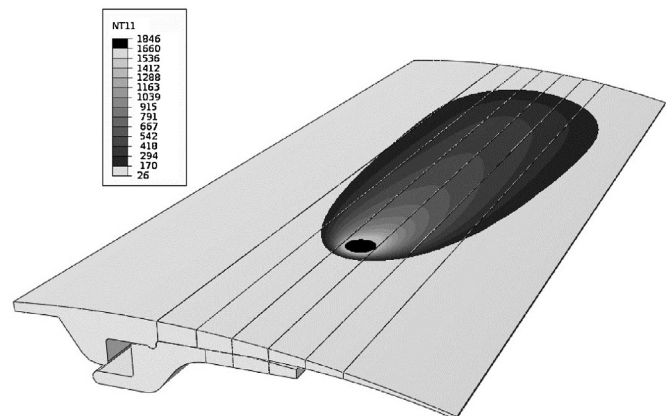

Fig. 10. Comparison between the FEA and measured temperature histories at the position of the thermocouples T#2 and T#6 for weld W#2.

Fig. 12. Steady state temperate field for the girth weld for the case with no heat transfer between the hemispheres and the retaining ring.
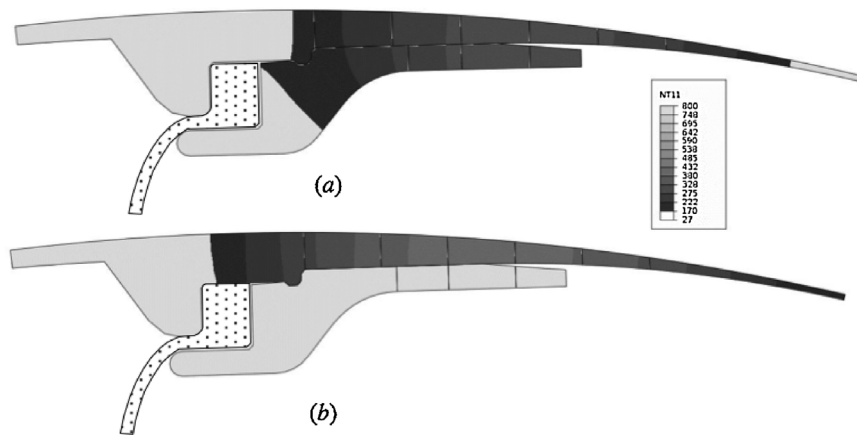
Fig. 13. Maximum extents of the T_c isotherm across the model thickness when (a) there is perfect continuity and heat transfer across the interface between the hemisphere inner wall and the retaining ring and (b) there is not heat transfer across the interface.

were considered: perfect continuity and heat transfer across the interface with contact conductance $k_c = \infty$, and an insulated interface with $k_c = 0$.

Fig. 12 depicts an overall view of the resultant steady-state temperature field for the case with $k_c = 0$. The limit values for the contour plots are set equal to the cure temperature of the diaphragm, $T_c = 170\,°C$, and the liquidus temperature of the titanium alloy, $T_{liquidus} = 1660\,°C$. In this way, the light-gray zones are those with temperatures lower than T_c and the black zone indicates the extent of the molten pool. The results in Fig. 12 and its counterpart for the case $k_c = \infty$ allowed to observe that the maximum

extents of the T_c isotherms occur at positions in the range from $w = -20\,mm$ to $w = -25\,mm$ behind the heat source.

The temperature distributions across the model thickness at the positions with the maximum extents of the T_c isotherms are shown in Fig. 13. It can be observed that the retaining ring has a strong influence on the temperature field in the zone of interest. When the ring is excluded of the analysis (the case with $k_c = 0$), a significant portion of the surface of the hemisphere wall in contact with the diaphragm exceeds the cure temperature, see Fig. 13b. On the other hand, when a perfect conductance is specified between the hemisphere walls and the retaining ring, the T_c isotherm spreads
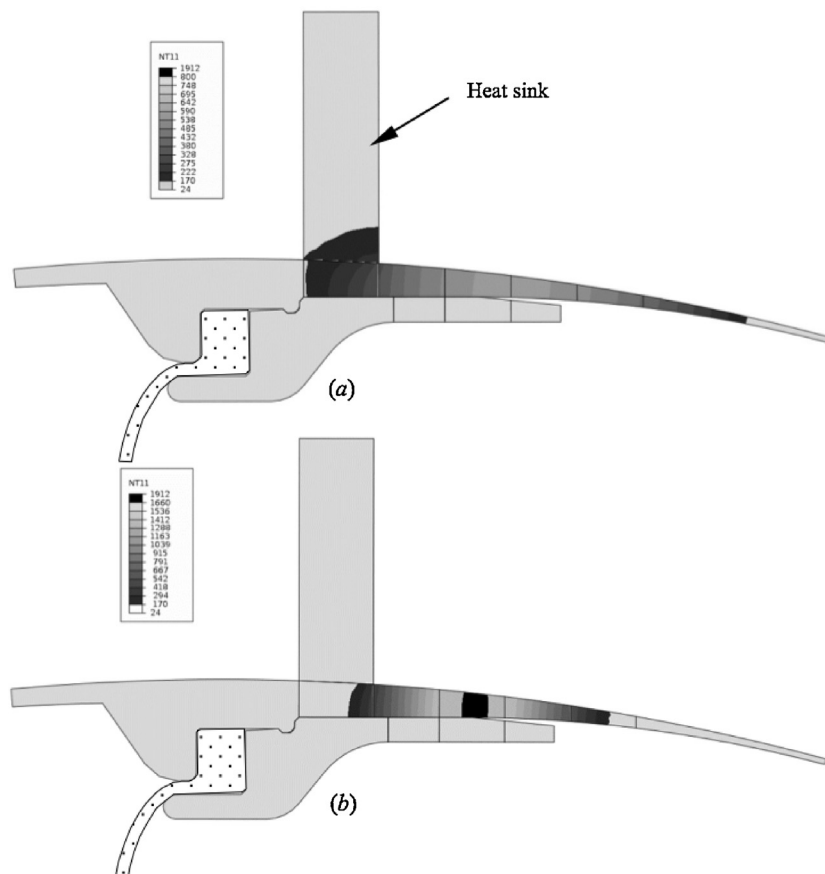

Fig. 14. Maximum extents of the T_c isotherm across the model thickness when (a) a there is perfect continuity and heat transfer across the interface between the hemisphere inner wall and the retaining ring and (b) there is not heat transfer across the interface.

up to the surface of the diaphragm, see Fig. 13a. This last hypothesis can be assimilated to the limiting condition to ensure the integrity of the diaphragm during welding.

Although the most conservative of the above analyses has led to a satisfactory result, practical issues might require to further adjusting the welding parameters. These issues are the differences in the thermal properties between the Ti–6Al–4V and the AISI 304 used for the model calibration, and the inherent errors and uncertainties associated to a FEA. In order to allow for an eventual increment of the heat input, it is proposed to include a heat sink to the welding setup in the form of a external ring around the pressurant hemisphere. The geometry of this new configuration is illustrated in Fig. 14. The ring is made of steel and has a cross-section with dimensions 30 mm × 90 mm. A thin layer of silicone grease, say 0.5 mm-thickness, is placed at the interface between the tank wall and the heat sink to favor the contact heat conduction. The thermal conductance of the grease layer is k_c = 8600 W/m^2 °C (Ozisik, 2002). In order to be on the safe side, the most conservative case with k_c = 0 is specified for the interface between the hemispheres and the retaining ring.

Fig. 14 depicts the results for the model with the heat sink. It can be observed from Fig. 14a that the heat sink is effective to lower the temperature in the vicinity of the diaphragm. The T_c isotherm is now around 25 mm apart from the surfaces in contact with the diaphragm. Fig. 14b illustrates the maximum extent of the molten pool, which occurs now at the position of heat source ($w = 0$). It can be observed that the molten pool extends across the hemisphere-wall thickness and reaches the retaining ring, what ensures the complete penetration of the weld.

6. Conclusions

The main results and contributions of this work are:

- An effective strategy based on the *STEP, *AMPLITUDE and *ANALYTICAL FIELD commands was devised to model the smooth displacement of the heat source using Abaqus. This strategy avoids the occurrence of "noisy" temperature results that are typical when the heat source is displaced using simple discrete steps.
- The standard deviation and efficiency of the heat input were calibrated using experiments performed on AISI 304 plates, the temperature of which were monitored using thermocouples and a thermographic camera. The molten-pool size was measured using macro etching. The values of the parameters were chosen to obtain the best predictions of the temperature field in the heat affected zone.

- The FE model of the tank shows that the retaining ring plays a key role on the temperature field in the vicinity of the diaphragm. It was found necessary to ensure a perfect continuity and heat transfer across the contact interface between the retaining ring and the inner wall of the hemispheres in order to keep the temperature of the diaphragm bellow the rubber cure temperature.
- It is proposed to include a heat sink in the welding setup in order to allow for eventual increments of the heat input due to further adjustments in the welding parameters. These adjustments would account for uncertainties in the material thermal properties and the welding setup. The complete penetration of the weld is ensured in every case.

References

Ballinger, I., Day, W., Tam, W., 1995. Review and history of PSI elastomeric diaphragm tanks. In: 31st AIAA/ASME/SAE/ASEE Joint Propulsion Conference and Exhibit, San Diego, CA, USA.
Carpenter Technology Corporation, 2000. Alloy data. Technical report, Wyomissing, PA, USA.
Charmchi, M., Martin, J., 1989. Natural convection heat transfer. In: Handbook of Applied Thermal Design. McGraw-Hill Book Company, New York, NY, USA.
Dassault Systems Simulia Corporation, 2009. Abaqus 6.9-1, Providence, RI, USA.
Goldak, J., Akhlaghi, M., 2005. Computational Welding Mechanics. Springer, New York, USA.
Goldak, J., Bibby, M., Moore, J., House, R., Patel, B., 1986. Computer modeling of heat flow in welds. Metallurgical and Materials Transactions B 17 (3), 587–600.
Grist, F., Farrell, W., Lawrence, G., 1993. Power sources for welding. In: ASM Handbook. Welding, Brazing and Soldering, vol. 6. ASM International, Materials Park, OH, USA.
Guyer, E., Golay, M., 1989. Elements of thermal design. In: Handbook of Applied Thermal Design. McGraw-Hill Book Company, New York, NY, USA.
Lindgen, L.-E., 2006. Numerical modelling of welding. Computer Methods in Applied Mechanics and Engineering 195, 6710–6736.
Lombera, G., Sedrani, A., de Vedia, L., 1989. Computational and experimental determination of temperature distribution in arc welding. In: David, S.A., Vitek, J.M. (Eds.), Recent Trends in Welding Science and Technology, 2nd Conference on Trends in Welding Research. ASM International, Gatlimburg, TN, USA, pp. 55–58.
Martin, J.G., Blanco-Muriel, M.J., 1989. Radiation heat transfer. In: Handbook of Applied Thermal Design. McGraw-Hill Book Company, New York, NY, USA.
MatWeb (last visited January 2012).
Moss, J., Stark, J., 2003. Propulsion systems. In: Spacecraft Systems Engineering. Wiley, Hoboken, NJ, USA, pp. 169–211.
Ozisik, M., 2002. Boundary Value Problems of Heat Conduction. Dover Publications, Mineola, NY, USA.
Pehlke, R., Jeyarajan, A., Wada, H., 1982. Summary of Thermal Properties for Casting Alloys and Mold Materials. National Technical Information Service, Washington, DC, USA.
Tsai, C., Tso, C., 1993. Heat flow in fusion welding. In: ASM Handbook. Welding, Brazing and Soldering, vol. 6. ASM International, Materials Park, OH, USA.